Topological Spinon Semimetals and Gapless Boundary States in Three Dimensions

Robert Schaffer, Eric Kin-Ho Lee, Yuan-Ming Lu, and Yong Baek Kim

Phys. Rev. Lett. **114**, 116803 — Published 17 March 2015

DOI: 10.1103/PhysRevLett.114.116803

Topological spinon semimetals and gapless boundary states in three dimensions

Robert Schaffer,[1] Eric Kin-Ho Lee,[1] Yuan-Ming Lu,[2,3] and Yong Baek Kim[1,4]

[1]*Department of Physics and Center for Quantum Materials, University of Toronto, Toronto, Ontario M5S 1A7, Canada.*
[2]*Department of Physics, University of California, Berkeley, CA 94720*
[3]*Materials Sciences Division, Lawrence Berkeley National Laboratory, Berkeley, CA 94720*
[4]*School of Physics, Korea Institute for Advanced Study, Seoul 130-722, Korea.*

(Dated: February 9, 2015)

Recently there has been much effort in understanding topological phases of matter with gapless bulk excitations, which are characterized by topological invariants and protected intrinsic boundary states. Here we show that topological semimetals of Majorana fermions arise in exactly solvable Kitaev spin models on a series of three dimensional lattices. The ground states of these models are quantum spin liquids with gapless nodal spectra of bulk Majorana fermion excitations. It is shown that these phases are topologically stable as long as certain discrete symmetries are protected. The corresponding topological indices and the gapless boundary states are explicitly computed to support these results. In contrast to previous studies of non-interacting systems, the phases discussed in this work are novel examples of gapless topological phases in interacting spin systems.

Introduction Theoretical prediction and experimental realization of topological insulators[1–3] (TIs) pushes our understanding of topological phenomena in condensed matter physics to a new level. Recently it was revealed that analogs of TIs exist in a large class of interacting boson and spin systems, dubbed "symmetry protected topological phases"[4, 5]. These topological phases are analogs of one another due to the existence of gapless surface states protected by symmetries, in spite of an energy gap for bulk excitations. Similar to TIs, a rich topology also exists in semimetals of weakly-interacting electrons featuring protected boundary excitations[6, 7], such as Weyl semimetals with surface Fermi arcs[8]. This raises a natural question: are there analogs of topological semimetals in interacting boson/spin systems, which harbor both gapless bulk excitations and protected surface states? Here we provide a positive answer to this question, in the ground states of the Kitaev model[9] on a series of three-dimensional trivalent lattices.

Motivated by recent discovery of the hyperhoneycomb ($\mathcal{H}$–0) and harmonic honeycomb ($\mathcal{H}$–1) iridates[10, 11], the Kitaev model on these lattices have been examined[12–15] and gapless $\mathbb{Z}_2$ spin-liquids with one-dimensional spinon nodal rings were found to be plausible ground states of these models[12–14]. In addition, a three-dimensional $\mathbb{Z}_2$ spin liquid with a two-dimensional Fermi surface was explored on the hyperoctagon lattice[16]. In this work, we show that the Majorana spinon nodal rings in the bulk of the gapless spin liquids on the $\mathcal{H}$–n lattices are topologically stable. Moreover, due to the bulk-boundary correspondence[17], these spin liquids exhibit protected gapless surface states in the form of dispersionless zero-energy flat bands.

Solution to Kitaev model: We first examine the bulk properties of the ground states on these lattices. Given a particular choice of the vectors $\hat{x}$, $\hat{y}$ and $\hat{z}$ (see Fig. 1), we define x, y and z bonds as those which are perpendicular to the associated directions. With this definition, each site shares one bond of each type with one of its three neighbours. As such, we define

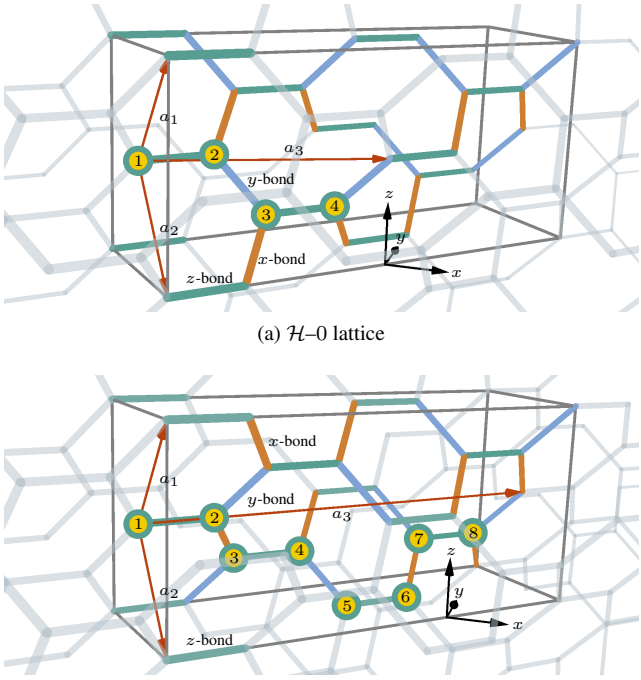

(a) $\mathcal{H}$–0 lattice

(b) $\mathcal{H}$–1 lattice

FIG. 1. (Color online) Unit cell, lattice vectors, sublattices, and coordinate systems for the $\mathcal{H}$–0 and $\mathcal{H}$–1 lattices. The conventional (orthorhombic) unit cells are drawn, while the sublattices in the primitive unit cells are labeled from 1 to $4n+4$. The x-, y-, and z-bonds within the conventional unit cell as defined in the Kitaev model are colored in orange, blue, and turquoise respectively.

the Kitaev Hamiltonian on these lattices as

$$\mathbf{H} = \sum_{\langle ij\rangle\in\alpha} J_\alpha \mathbf{S}_i^\alpha \mathbf{S}_j^\alpha, \tag{1}$$

where α denotes the bond type of bond ij, and the sum runs over nearest neighbour bonds. We take J_α to be the same over all bonds of type α and $J_x = J_y$ for simplicity, which preserves the crystal symmetries of the lattices.

This model can be solved exactly by introducing four Majorana spinons $\{b^x, b^y, b^z, c\}$ at each site and replacing $\mathbf{S}_i^\alpha = ib_i^\alpha c_i$[9]. The operators $u_{ij} = ib_i^\alpha b_j^\alpha = -u_{ji}$ (where ij is an α bond) commute with one another and the Hamiltonian, thus they define conserved quantities that take on the values of ± 1 on each bond. These u_{ij} are not gauge invariant. However, products of these operators over closed loops, which correspond to fluxes of the Z_2 gauge field, are gauge invariant[9]. By choosing a configuration of $\{u_{ij}\}$, the fluxes are fully determined and the Hamiltonian becomes quadratic in terms of the c fermions. The ground state can be found by solving the quadratic Hamiltonians corresponding to all possible flux configurations (or flux *sectors*) and identifying the flux sector that yields the lowest energy state. Other flux sectors are important when considering the high-energy excitations and dynamic properties of the model[18, 19]; however, we will limit our focus to the ground state properties of these models.

Unlike the 2D honeycomb lattice, both the hyperhoneycomb (*i.e.* $\mathcal{H}$–0) and $\mathcal{H}$–1 lattices possess loops without mirror symmetries. As such, Lieb's theorem [20] cannot determine the flux passing through these loops in the ground state. We performed a brute-force search throughout all flux sectors compatible with an 8-fold enlarged unit cell and the results suggest that the ground state on the hyperhoneycomb lattice belongs to the zero-flux sector, which agrees with previous work[12]. In contrast, on the $\mathcal{H}$–1 lattice, we find that the ground state flux sector differs for different values of $\delta = J_z/J_x$. At the isotropic point $\delta = 1$, a particular flux configuration with π flux passing through a subset of the loops appears to be the ground state flux sector (hereafter, we label it as the "π-flux sector"). Upon increasing δ, the zero-flux sector becomes energetically favorable. We will first focus on the zero-flux sectors on the hyperhoneycomb and $\mathcal{H}$–1 lattices and defer the more involved analysis of the π-flux sector on the $\mathcal{H}$–1 lattice for later.

Bulk Majorana spectrum in the zero-flux sector: Due to the bipartite nature of both the hyperhoneycomb and $\mathcal{H}$–1 lattices, the Hamiltonian in any flux sector takes the off-diagonal form

$$\mathbf{H}_n^\Phi = \sum_k \vec{c}_{n,-k}^{\,T} H_{n,k}^\Phi \vec{c}_{n,k} \tag{2}$$

$$H_{n,k}^\Phi = \begin{bmatrix} 0 & -iD_{n,k}^\Phi \\ i\left(D_{n,k}^\Phi\right)^\dagger & 0 \end{bmatrix}, \tag{3}$$

where n refers to the n^{th}-harmonic honeycomb, Φ labels the flux sector, and $\vec{c}_{n,k}$ is the vector of the Fourier transforms of the c Majorana fermions ordered by the odd sublattices followed by the even sublattices (See Supplemental Material [21] for definition of lattice vectors, unit cell, and sublattice conventions). In the zero-flux sector, we can choose the gauge where $u_{ij} = 1$ when i is an even sublattice and j is an odd sublattice. Consequently, the D^0-matrices for the hyperhoneycomb and $\mathcal{H}$–1 lattices are

$$D_{0,k}^0 = \begin{bmatrix} J_z & A_k e^{ik_3} \\ B_k & J_z \end{bmatrix}, D_{1,k}^0 = \begin{bmatrix} J_z & 0 & 0 & A_k e^{ik_3} \\ A_k^* & J_z & 0 & 0 \\ 0 & B_k & J_z & 0 \\ 0 & 0 & B_k^* & J_z \end{bmatrix}, \tag{4}$$

where $A_k = J_x(1 + e^{-ik_1})$, $B_k = J_x(1 + e^{-ik_2})$ with $k_i = \vec{k} \cdot \vec{a}_i$, and $\vec{a}_i$ are the lattice vectors.

Each of the zero-flux sectors of both hyperhoneycomb and $\mathcal{H}$–1 lattices possesses gapless spinon excitations in the bulk that form a nodal ring in the 3D Brillouin zone (BZ). The off-diagonal block form of H_n^Φ ensures that the zero-modes of H_n^Φ are determined by $\det(D_{n,k}^\Phi) = 0$. For the zero-flux phase of the hyperhoneycomb and $\mathcal{H}$–1 lattices, these conditions are

$$\mathcal{H}\text{–}0: \qquad 4\cos\frac{k_1}{2}\cos\frac{k_2}{2} = \delta^2 e^{-i(k_3 - \frac{k_1}{2} - \frac{k_2}{2})}, \tag{5}$$

$$\mathcal{H}\text{–}1: \qquad \left|4\cos\frac{k_1}{2}\cos\frac{k_2}{2}\right| = \delta^2 e^{-ik_3}. \tag{6}$$

For values of $\delta < 2$, a continuous set of solutions exist for each of Eq. (5) and Eq. (6), which defines the nodal ring. We have illustrated the locations of the nodal rings for the isotropic case $\delta = 1$ in Fig. 2a and Fig. 2b.

Topological invariants of the nodal ring: The nodal rings present in the zero-flux sectors of the hyperhoneycomb and $\mathcal{H}$–1 models are topologically stable. To see this, we first define the time-reversal (TR) and particle-hole (PH) symmetry operators, whose unitary components satisfy the following relations

$$H_k = \epsilon_U U H_{-k}^T U^{-1}, \quad UU^\dagger = \mathbb{I}, \quad U^T = \eta_U U, \tag{7}$$

where H_k is the Hamiltonian matrix, ^{T} is the matrix transpose, $\mathbb{I}$ is the identity matrix, $U = T, P$ for TR/PH respectively, $\epsilon_U = \pm 1$ for TR/PH, and $\eta_U = \pm 1$. The presence of both TR and PH ensures that $\mathbf{S} = \mathbf{TP}$ is a chiral (or sublattice) symmetry of the system, which satisfies $\{\mathbf{S}, \mathbf{H}_n^\Phi\} = 0$ (where boldface letters denote operators).

In the case of the hyperhoneycomb and $\mathcal{H}$–1 lattices, we find for the zero-flux sector

$$T_n^0 = S_n^0 = \sigma_z \otimes \mathbb{I}_{2n+2}, \quad P_n^0 = \mathbb{I}_{4n+4}, \tag{8}$$

where σ are the Pauli matrices, $\otimes$ is the tensor product of matrices, and $\mathbb{I}_m$ is the $m \times m$ identity matrix. In both systems, $\eta_T = \eta_P = +1$, which implies that $H_{n,k}^0$ belongs to symmetry class BDI based on the classification of topologically stable Fermi surfaces (FS's)[17, 22]. The topological stability of a nodal ring in three-dimensional systems of class BDI is characterized by the following integer-valued topological invariant (winding number)

$$\nu = \frac{1}{4\pi i}\oint \mathrm{d}k \mathrm{Tr}[D_{\mathbf{k}}^{-1}\partial_k D_{\mathbf{k}} - (D^\dagger)_{\mathbf{k}}^{-1}\partial_k D_{\mathbf{k}}^\dagger], \tag{9}$$

where the integral is taken along a path around the nodal ring.

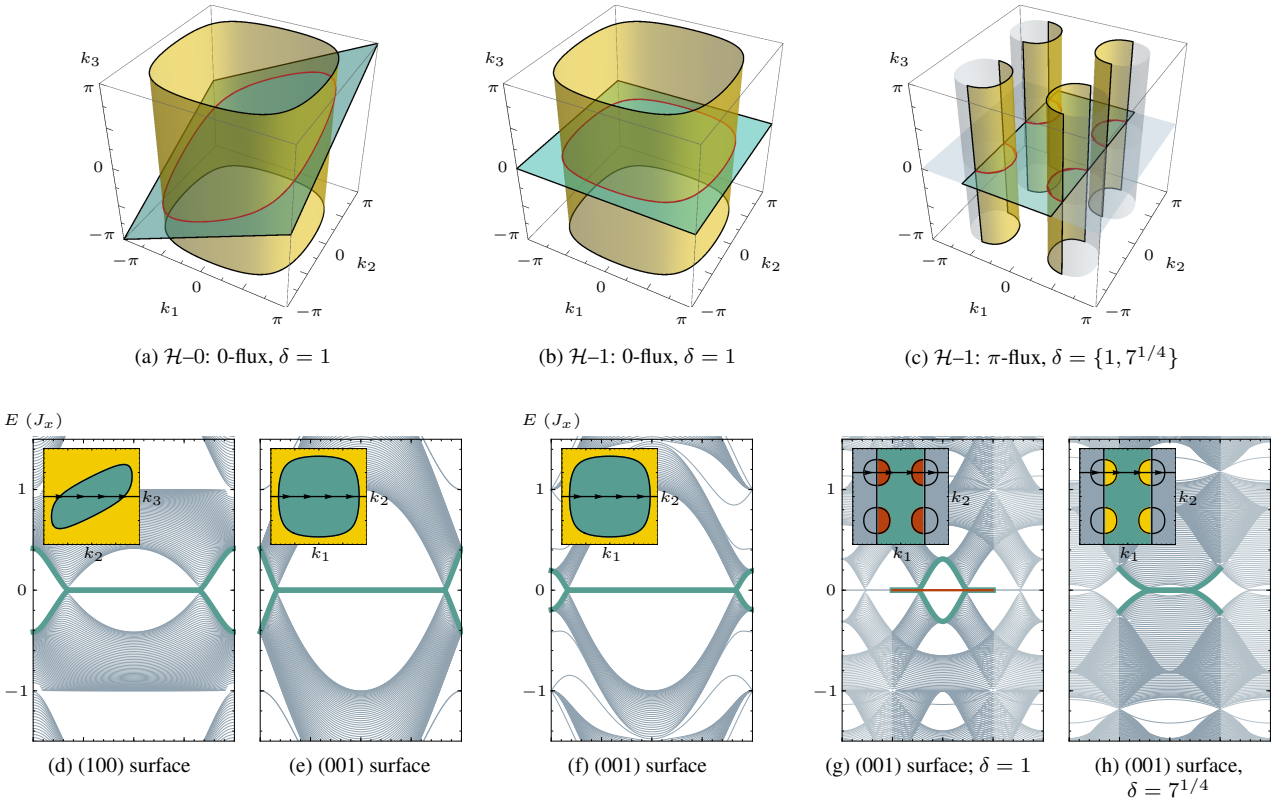

(a) $\mathcal{H}$–0: 0-flux, $\delta = 1$ (b) $\mathcal{H}$–1: 0-flux, $\delta = 1$ (c) $\mathcal{H}$–1: π-flux, $\delta = \{1, 7^{1/4}\}$

(d) (100) surface (e) (001) surface (f) (001) surface (g) (001) surface; $\delta = 1$ (h) (001) surface, $\delta = 7^{1/4}$

FIG. 2. (Color online) Position of nodal rings, surface spectra, and winding numbers. In Figs. 2a-2c, the red lines show the location of the nodal rings of the indicated lattice, flux sector, and $\delta = J_z/J_x$. The red lines are the intersections of the yellow and turquoise surfaces, which are the LHS $= 1$ and RHS $= 1$ of Eq. 5, Eq. 6, and Eq. 11. In Fig. 2c, the first Brillouin zone spans the region $-\pi/2 < k_1 \leq \pi/2$ due to doubling of the unit cell in the π-flux sector. Figs. 2d-2h show the surface spectra along one-dimensional momentum cuts on the various lattices and flux sectors, while the insets within indicate the location of the momentum cuts and projection of the nodal ring on the surfaces indicated. The colors in the insets correspond to the winding numbers, where yellow, turquoise, and red are $\nu = 0, \pm 1$, and ± 2 respectively. When $\nu \neq 0$, as shown in Figs. 2d-2h, we find the presence of zero-energy surface flat bands with $|\nu|$-fold degeneracy, due to the bulk-boundary correspondence.

We can deform the path into two pieces: one passing through the inside of the nodal ring and one outside. Integrating Eq. 9 in the k_3 direction along the lines $k_1 = k_2 = 0$ (inside the nodal ring) and $k_1 = k_2 = \pi$ (outside the nodal ring), we find a nontrivial winding number $\nu = 1$ inside the nodal ring but a trivial one ($\nu = 0$) outside (See Supplemental Material [21] for details). As a result, the nodal ring is characterized by a topological index $\nu = \pm 1$ and is hence topologically stable.

Surface spectra: The surface spectra of the hyperhoneycomb and $\mathcal{H}$–1 lattices is expected to possess zero-energy flat bands due to the bulk-boundary correspondence[17], as long as the bulk nodal ring has finite projection in the surface BZ. At the momenta corresponding to the projection of the nodal ring on a surface, the change in the number of flat bands must be the same as the topological index ν of the ring.

For the hyperhoneycomb lattice, we examine the spectra associated with the (100) and (001) surfaces in Fig. 2d and 2e (the surface (010) is related to the (100) surface by a glide plane symmetry, hence it is not shown). Since the nodal ring has finite projection along k_1 and k_3, flat bands at zero energy are expected in both surface spectra. Indeed, we see $\nu = 1$ within the area enclosed by the projection of the nodal ring. Plotting the surface spectra along momentum paths that cut through the nodal ring projections, we see the presence of flat bands where the winding number is ± 1. In contrast, the nodal ring in the $\mathcal{H}$–1 lattice only has finite projection along the k_3 direction. Therefore, only the (001) surface spectrum possesses zero energy flat bands, which can be seen in Fig. 2f.

Analysis of the π-flux sector: The above analysis can be performed analogously in the π-flux sector on the $\mathcal{H}$–1 lattice; here we summarize the main results. The description of the π-flux sector requires doubling of the unit cell in the a_1 direction (See Supplemental Material [21] for definition of the enlarged unit cell and $D^{\pi}_{1,k}$). Due to the enlarged unit cell, the TR, PH, and chiral symmetry operators are now given by

$$T^{\pi}_n = S^{\pi}_n = \sigma_z \otimes \mathbb{I}_{4n+4}, \quad P^{\pi}_n = \mathbb{I}_{8n+8} \tag{10}$$

with $n = 1$. Since $\eta_T = \eta_P = +1$, H^{π}_k still belongs to class BDI and its nodal rings are associated with $\mathbb{Z}$-valued topological invariants.

When $0 < \delta < 2^{3/4}$, the bulk spectrum possesses two nodal rings that satisfy

$$16 \sin^2 k_1 \sin^2 k_2 = 8e^{-ik_3}\delta^4 - e^{-2ik_3}\delta^8 \qquad (11)$$

where $-\frac{\pi}{2} \leq k_1 < \frac{\pi}{2}$ due to the doubling of the unit cell. The parameter point $\delta' \equiv \sqrt{2}$ is unique: upon increasing δ towards this value, the two nodal rings shrink towards $k'_{\pm} = (\frac{\pi}{2}, \pm\frac{\pi}{2}, 0)$. At δ', the nodal rings turn into Dirac points at $k'_{\pm}$. Upon further increasing δ beyond δ', the nodal rings return and expand. For $\delta < \delta'$, $\nu = \pm 2$ inside the nodal rings and $\nu = \pm 1$ outside the nodal rings. On the other hand, when $\delta' < \delta < 2^{3/4}$, ν inside the nodal rings decreases to 0, while ν remains as ± 1 outside the nodal rings. The surface spectra of these cases are illustrated in Fig. 2g and 2h.

Generalization to the $\mathcal{H}$–n lattice: The above results for the zero-flux sector can be straightforwardly extended to all the $\mathcal{H}$–n lattices[11]. In fact, many of the results remain the same: the position of the nodal ring for even-n lattices is given by Eq. 5, while for the odd-n lattices it's given by Eq. 6. The operators T^0_n, P^0_n, and S^0_n are still defined by Eq. 8 where n is now arbitrary, therefore the whole family of $H^0_{n,k}$ belongs to class BDI. For the calculation of the winding number, we have

$$\mathrm{Tr}[D^{-1}_{n,k_3}\partial_{k_3}D_{n,k_3}] = \frac{-ie^{ik_3}}{(\delta/2)^{2n+2} - e^{ik_3}} \qquad (12)$$

along the line $k_1 = k_2 = 0$ for all the $\mathcal{H}$–n lattices. In addition, $D^0_{n,k}$ is constant along k_3 when $k_1 = k_2 = \pi$. Hence, the winding number is always 1 and 0 inside and outside the nodal ring, respectively.

For the π-flux sector, the TR, PH, and chiral symmetry operators are still defined by Eq. 10 for arbitrary n, and the spinon Hamiltonian $H^{\pi}_{n,k}$ belongs to the BDI class. Other aspects of the Hamiltonian are less generalizable, however. The zero modes of the bulk Hamiltonian do not follow a generalized form; however, we have numerically verified that two nodal rings are present for $n < 15$. The point $\delta = \delta'$ remains as a special point where the two nodal rings collapse to two points. Like the $\mathcal{H}$–1 model, for $\delta < \delta'$, $\nu = 2(1)$ inside (outside) the nodal rings, while for $\delta > \delta'$ within the gapless phase, $\nu = 0(1)$ inside (outside) the nodal rings. Therefore, the spinon nodal rings in the bulk and surface flat bands are topologically protected.

Summary and Discussion: A nearest-neighbor tight-binding Hamiltonian of spinless electrons hopping on a $\mathcal{H}$–n lattice will have the same band structure as the zero-flux sector. With PH, chiral, and charge conservation symmetry, it also belongs to symmetry class BDI, with the unitary component of the time-reversal and particle-hole symmetry operators exchanged with respect to the Kitaev spin liquid. This means a half-filled electron system on the $\mathcal{H}$–n lattice can also host topologically stable nodal rings in the bulk and symmetry-protected flat bands on the surface.

Although this work focuses on the hyperhoneycomb and $\mathcal{H}$–n lattices, our analysis applies to Kitaev models on any bipartite and trivalent lattice. Generally, the spinon band structure of any bipartite-lattice Kitaev model belongs to symmetry class BDI, whose Hamiltonian has the form of Eq. (2) independent of the flux sector. Since the Majorana spinon FS's are determined by two real equations

$$\mathrm{Re}\,[\det(D_k)] = \mathrm{Im}\,[\det(D_k)] = 0, \qquad (13)$$

a d-dimensional lattice will generically give $(d-2)$-dimensional spinon FS's[16]. Similar to nodal rings in three-dimensional lattices, each $(d-2)$-dimensional FS in the d-dimensional BZ is classified by an integer-valued topological invariant ν for symmetry class BDI. A non-zero ν will imply the stability of the spinon FS and protected surface flat bands.

A simple example is the original Kitaev model on the honeycomb lattice[9]. Majorana spinons in the gapless $\mathbb{Z}_2$ spin liquid ground state have a graphene-like band structure, with a pair of topologically stable point nodes with $\nu = \pm 1$. This leads to localized spinon flat bands on the boundaries.

An exception occurs when the surfaces defined by the two constraints in Eq. (13) coincide, such as the case of the hyperoctagon lattice[16] where a 2D FS of Majorana spinons arises. The FS is characterized by a $\mathbb{Z}_2$ topological index of class BDI and there are no surface flat bands associated with it[17].

Near the isotropic limit of the $\mathcal{H}$–n models, we find the presence of nodal rings. Through numerical and analytical calculations, we find that the winding numbers around these rings are ± 1 in all cases that we examined. As required by the bulk-boundary correspondence, we find surface flat bands protected by the present symmetries.

In the strongly anisotropic limit, the nodal rings disappear and the ground states of the $\mathcal{H}$–n models become gapped quantum spin liquids. These gapped phases also have a non-trivial topology, characterized by 1D weak indices[23] of symmetry class BDI. The physical consequence of this weak index is that the surface flat bands of Majorana spinons will persist even when we enter the gapped phase, as long as translation symmetry is preserved[24, 25]. Once we break TR and hence chiral symmetry (leading to symmetry class D), the surface flat bands gain a dispersion and the bulk line node can gain a gap.

While this manuscript focuses on the properties of the model in the ground state, we expect the results to extend to small finite temperatures[15]. A gap exists to flux excitations in the model, resulting in the number of such excitations being exponentially supressed in the low temperature limit. As such, the band structure of the spinon excitations is robust for small T, and the flat surface band structure should be detectable experimentally in such a system. Comparing the results of thermal transport measurements taken across different surfaces allows one to identify the presence of such surface modes, as these are absent on surfaces perpendicular to the bulk nodal ring. In addition, due to the divergence in the density of states on the surface at zero energy, we expect the surface contribution to the specific heat will dominate the T^2 bulk signal at sufficiently low temperatures[26]. By tuning the aspect ratio between the surface with flat bands and the other

surfaces (and the bulk), one may be able to isolate this contribution, providing strong evidence of the presence of these topological surface bands.

We thank Yige Chen for discussions. YML and YBK acknowledge the hospitality of the Aspen Center for Physics (NSF Grant No. PHYS- 1066293), where some part of this work was performed. This research was supported by the NSERC, CIFAR and Centre for Quantum Materials at the University of Toronto (RS,EKHL,YBK), and by Office of BES, Materials Sciences Division of the U.S. DOE under contract No. DE-AC02-05CH11231 (YML).

[1] M. Z. Hasan and C. L. Kane, Rev. Mod. Phys. **82**, 3045 (2010).
[2] M. Z. Hasan and J. E. Moore, Annu. Rev. Condens. Matter Phys. **2**, 55 (2011), ISSN 1947-5454.
[3] X.-L. Qi and S.-C. Zhang, Rev. Mod. Phys. **83**, 1057 (2011).
[4] X. Chen, Z.-C. Gu, Z.-X. Liu, and X.-G. Wen, Phys. Rev. B **87**, 155114 (2013).
[5] T. Senthil, ArXiv e-prints (2014), 1405.4015.
[6] A. M. Turner and A. Vishwanath, ArXiv e-prints (2013), 1301.0330.
[7] O. Vafek and A. Vishwanath, Annu. Rev. Condens. Matter Phys. **5**, 83 (2014), ISSN 1947-5454.
[8] X. Wan, A. M. Turner, A. Vishwanath, and S. Y. Savrasov, Phys. Rev. B **83**, 205101 (2011).
[9] A. Kitaev, Annals of Physics **321**, 2 (2006), ISSN 0003-4916.
[10] T. Takayama, A. Kato, R. Dinnebier, J. Nuss, and H. Takagi, ArXiv e-prints (2014), 1403.3296.
[11] K. A. Modic, T. E. Smidt, I. Kimchi, N. P. Breznay, A. Biffin, S. Choi, R. D. Johnson, R. Coldea, P. Watkins-Curry, G. T. McCandless, et al., Nat CommunRobertSchaffer **5**, (2014).
[12] S. Mandal and N. Surendran, Phys. Rev. B **79**, 024426 (2009).
[13] E. K.-H. Lee, R. Schaffer, S. Bhattacharjee, and Y. B. Kim, Phys. Rev. B **89**, 045117 (2014).
[14] I. Kimchi, J. G. Analytis, and A. Vishwanath, ArXiv e-prints (2013), 1309.1171.
[15] J. Nasu, T. Kaji, K. Matsuura, M. Udagawa, and Y. Motome, Phys. Rev. B **89**, 115125 (2014).
[16] M. Hermanns and S. Trebst, Phys. Rev. B **89**, 235102 (2014).
[17] S. Matsuura, P.-Y. Chang, A. P. Schnyder, and S. Ryu, New Journal of Physics **15**, 065001 (2013), ISSN 1367-2630.
[18] G. Baskaran, Saptarshi Mandal, and R. Shankar, Phys. Rev. Lett. **98**, 247201 (2007).
[19] J. Knolle, D. L. Kovrizhin, J. T. Chalker, and R. Moessner, Phys. Rev. Lett. **112**, 207203 (2014).
[20] E. H. Lieb, Phys. Rev. Lett. **73**, 2158 (1994).
[21] See Supplemental Material for definition of lattice, details of the winding number calculations, and definition of the π-flux phase.
[22] Y. Zhao and Z. Wang, Physical Review Letters **110**, 240404 (2013).
[23] Y. Ran, ArXiv e-prints 1006.5454 (2010), 1006.5454.
[24] S.-P. Kou, M. Levin, and X.-G. Wen, Phys. Rev. B **78**, 155134 (2008).
[25] G. Y. Cho, Y.-M. Lu, and J. E. Moore, Phys. Rev. B **86**, 125101 (2012).
[26] T. T. Heikkil, N.-B. Kopnin, and G. E. Volovik, JETP Letters **94**, 233 (2011).